

Spatial Analysis of Airborne Geophysical Data Applied to Geological Mapping and Mineral Prospecting in the Serra Leste Region, Carajás Mineral Province, Brazil

Carlos Roberto de Souza Filho · Alfredo Rossetto Nunes ·
Emilson Pereira Leite · Lena Virgínia Soares Monteiro ·
Roberto Perez Xavier

Received: 19 April 2007 / Accepted: 28 February 2008 / Published online: 15 March 2008
© Springer Science+Business Media B.V. 2008

Abstract The Serra Leste region, located in the northeast portion of Carajás Mineral Province (PA), hosts important chrome-PGE, Au–Pd–Pt, Cu–Mo–Au, iron, and manganese deposits and occurrences related to different geological settings. We present a regional prospective model with focus on PGE mineralizations based on airborne geophysics (magnetometry, gamma-ray spectrometry and time domain electromagnetometry) and geological data. Geological and geophysics data analysis indicate a plausible correspondence between areas with meta-mafic–ultramafic rocks and low values in gamma spectrometry, mainly for the thorium channel. The meta-ultramafic units of the complexes, the main host rock of the PGE mineralization, are well defined by analytic signal from the anomalous magnetic field and by the apparent conductance anomalies derived from the GEOTEM system. The combination of the derivative products with updated geological data of the Serra Leste region and PGE-Luanga deposit enable to establish a regional prospective model for PGE and the identification of new targets within the studied area.

Keywords Spatial analysis · Airborne potential field data · Mineral Prospecting · Platinum group elements

1 Introduction

The Carajás Mineral Province (CMP), Pará state, Brazil, is a polymetallic province that represents one of the best endowed mineral districts in the world including iron (e.g., N4, N5), iron oxide–copper–gold (e.g., Sossego, Salobo, Cristalino, Igarapé Bahia), manganese (e.g., Azul and Buritirama), nickel (e.g., Vermelho, Onça-Puma), chrome-PGE e.g. Luanga), Au–Pd–Pt (e.g. Serra Pelada), Cu–Mo–Au deposits (e.g. Serra Verde; Villas and Santos 2001).

C. R. de Souza Filho (✉) · A. R. Nunes · E. P. Leite · L. V. S. Monteiro · R. P. Xavier
Instituto de Geociências, Universidade Estadual de Campinas, P.O. Box 6152, 13083-970 Campinas,
SP, Brazil
e-mail: beto@ige.unicamp.br

The Serra Leste area, located in the northeast portion of the CMP, between the parallels 634.000 E and 666.000 E and the meridians 9.325.000 N and 9.347.400 N (Zone 22S; Fig. 1), represents a key area in this province due to its diversity of ore deposit types. It comprises several of the world-class deposits found in the CMP, including: (i) the Serra Pelada Au–Pd–Pt deposit hosted by the ~2.68 Ga Rio Fresco Group/Águas Claras Formation (Cabral et al. 2002a, b); (ii) Cu–Mo–Au deposits (e.g., Serra Verde; Villas and Santos 2001) in meta-volcanic rocks of the Rio Novo Group close to the contact with the 2.76 Ga Estrela Granite (Marschik et al. 2005); (iii) iron deposits in rocks of the 2.76 Ga Itacaiúnas Supergroup (e.g., Serra Leste); and (iv) manganese deposits (e.g., Sereno; Coelho and Rodrigues 1986) hosted by the Rio Fresco Group.

The Serra Leste area also hosts chrome–PGE deposits associated with mafic–ultramafic complexes (e.g. Luanga; Suita 1988). Luanga chromitites are characterized by their high Pd/Ir ratios and PGE contents. They have elevated Pt concentrations (up to 8,900 ppb; Diella et al. 1995); which are comparable to those of layered mineralized complexes, such as Stillwater Complex, Montana, and UG2, Bushveld Complex (Diella et al. 1995; Girardi et al. 2006).

The lack of outcrops, thick soil cover and dense Amazon forest in this area makes airborne geophysics a required tool for geological mapping and mineral exploration. This work aims to integrate geological and high resolution airborne geophysical data, in order to obtain a prospective model for the PGE mineralizations in the Serra Leste area. Airborne magnetic, gamma-ray spectrometric and electromagnetic (GEOTEM) data combined with geological and topographic maps are used to reach the proposed goal. Known mineral occurrences and deposits were used to compose the prospective model.

2 Regional Geology of the Carajás Mineral Province

The Carajás Mineral Province (CMP) is located in the southern part of the Amazon Craton, which is one of the largest cratonic areas in the world (Fig. 1). The Archean basement includes tonalitic to trondhjemitic gneiss and migmatite of the Xingu Complex ($2,974 \pm 15$ Ma; Machado et al. 1991) and granulite of the Pium Complex. In the latter, SHRIMP zircon ages of $3,002 \pm 14$ Ma and $2,861 \pm 12$ Ma are considered as representative of the parent magmatic rock and the granulite facies metamorphism, respectively (Pidgeon et al. 2000). The basement rocks are overlain by meta-volcanic-sedimentary units of the Rio Novo Group (Hirata et al. 1982) and the 2.73–2.76 Ga Itacaiúnas Supergroup (Igarapé Salobo, Igarapé Pojuca, Grão Pará, and Igarapé Bahia groups; Wirth et al. 1986; Docegeo 1988; Machado et al. 1991; Trendall et al. 1998; Krymsky et al. 2002; Galarza et al. 2003; Pimentel et al. 2003; Tallarico et al. 2005). These volcanic-sedimentary sequences comprise variably deformed and metamorphosed (low greenschist to amphibolite facies) basic and felsic volcanic and pyroclastic rocks, iron formations, and clastic sedimentary rocks (Wirth et al. 1986; Hirata et al. 1982; Docegeo 1988; Machado et al. 1991).

The Rio Novo Group and the Itacaiúnas Supergroup are in turn overlain by a low-grade metamorphic, sedimentary sequence that includes conglomerate with iron formation, quartzite and siltstone clasts within a foliated quartz-sericite matrix, sandstone, locally manganese-rich, dolomitic marble with lenses of talc-chlorite-rich rocks, carbonaceous siltstone, and sericite-rich quartzites (Tallarico et al. 2000). This unit, known as the Rio Fresco Group (Docegeo 1988) or the Águas Claras Formation (Nogueira 1985; Araújo et al. 1988), was deposited in a shallow-marine to fluvial environment. Dating of detrital zircon in sandstones ($2,681 \pm 5$ Ma; Trendall et al. 1998) and meta-gabbro sills ($2,645 \pm 12$ Ma and

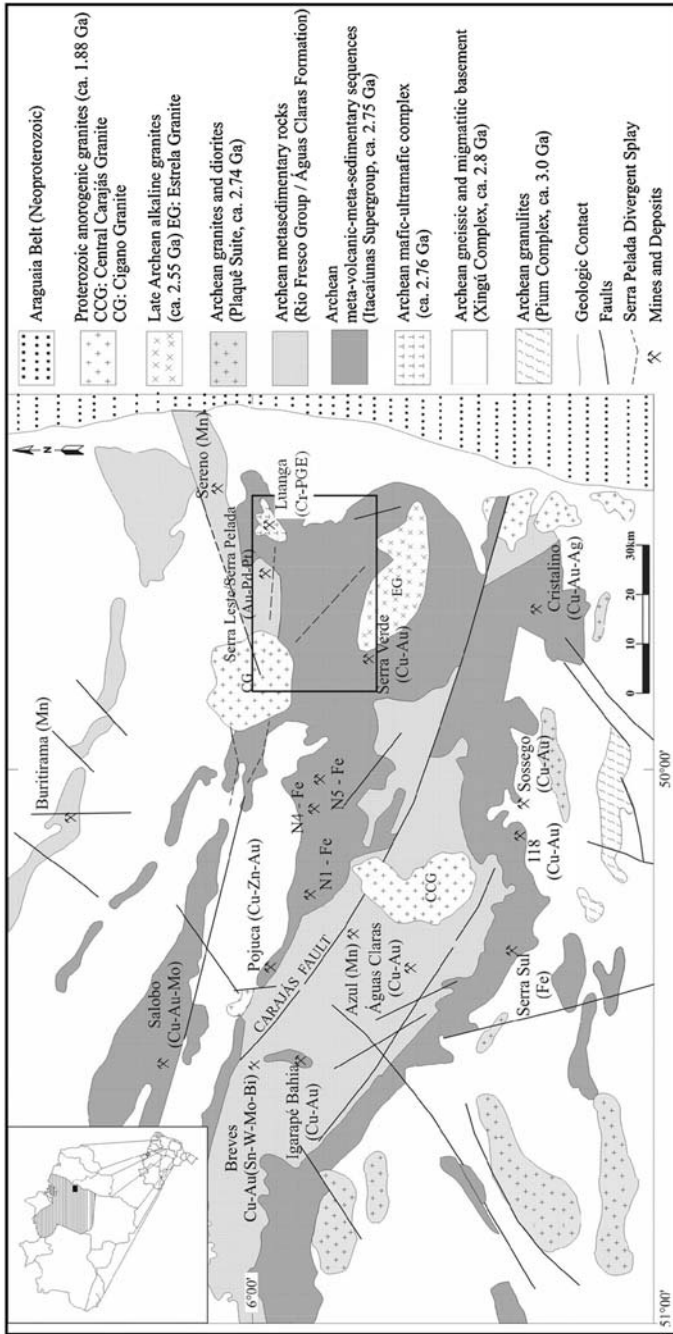


Fig. 1 Geological map of the Carajás Mineral Province (CMP), including the location of the main mineral deposits (adapted from Docego 1988). The Serra Leste area is highlighted in the eastern portion of the CMP

2,708 ± 37 Ma; Dias et al. 1996; Mougeot et al. 1996) constrains the age of the Águas Claras Formation to the Archean.

The complex structural evolution of the Carajás Archean units have been attributed to the development of regional E–W trending, steeply dipping fault zones that show evidence of several episodes of reactivation (Holdsworth and Pinheiro 2000). The Itacaiúnas sinistral transpressive strike-slip ductile shear zone was formed at 2.85–2.76 Ga. Dextral transtension led to the development of the Carajás and Cinzento strike-slip fault systems between 2.7 and 2.6 Ga. A sinistral transpressional regime evolved at about 2.6 Ga resulted in moderate to strong deformation of the rocks immediately adjacent to the Carajás and Cinzento fault systems (Holdsworth and Pinheiro 2000).

Syntectonic alkaline granites (2.76–2.74 Ga Estrela, Plaqué, Planalto and Serra do Rabo; Dall’Agnol et al. 1997; Avelar et al. 1999; Barros et al. 2001, 2004) intrude the Itacaiúnas and Rio Novo meta-volcanic-sedimentary sequence. Monzogranite dated at 2,688 ± 11 Ma could represent volcanic-arc calc-alkaline magmatism, although these data should be interpreted carefully, due to the hydrothermal alteration overprint observed in the dated rock (Barros et al. 2001).

Late Archean alkaline, meta-aluminous granite (e.g., Old Salobo, 2,573 ± 2 Ma; Machado et al. 1991; Itacaiúnas, 2,560 ± 37 Ma; Souza et al. 1996) also occur in the province. Other Archean intrusions include the Vermelho, Onça, Jacaré-Jacarezinho and Luanga (2,763 ± 6 Ma, Machado et al. 1991) mafic–ultramafic layered complexes, as well as 2.76–2.65 Ga gabbro dikes and sills (Galarza et al. 2003; Pimentel et al. 2003). Extensional events in the Paleoproterozoic were accompanied by widespread emplacement of within-plate A-type, alkaline to subalkaline granites (e.g., ~1.87–1.88 Ga Serra dos Carajás, Cigano, Cigano, Pojuca, Young Salobo, Musa, Jamon, Seringa, Velho Guilherme, and Breves; Machado et al. 1991; Dall’Agnol et al. 1994, 1999a, b, 2005; Macambira and Lafon 1995; Teixeira et al. 2002; Tallarico et al. 2004) and dike swarms throughout the CMP.

The province was also affected by other magmatic events represented by late diabase, diorite, and gabbro dikes, whose ages are uncertain.

3 Geology of the Serra Leste Area

A geological map produced by Veneziani and Okida (2001) for the Serra Leste region was enhanced in this work, based on new geophysical and extensive field data. Among the main additions and modifications to previous geologic maps of the area are: (i) densification of structural information; (ii) mapping of banded iron-formations in the central-north portion of the study area; (iii) detection of lateritic soils between Tertiary and Quaternary detritic sediments in the north and northwest of the area, which unraveled the presence of iron-formations in the Rio Novo Group; (iv) mapping of gabbroic-granophyric dikes embedded in NNW-oriented fracture zones that truncates all lithostratigraphic units of the Itacaiúnas Supergroup (Fig. 2).

Amphibolites, schist, meta-graywacke, mafic tholeiitic meta-volcanic rocks, diorites, and gabbros of the Rio Novo Group, together with mafic schist and iron formation of the Grão Pará Group (Itacaiúnas Supergroup) are the dominant lithologies at Serra Leste.

The Rio Novo Group was intruded by mafic–ultramafic complexes, such as Luanga, Luanga Sul, Orion, Afrodite, Formiga, North Luanga, Pegasus, and Centauro. The main mafic–ultramafic complex is represented by the chromite- and PGE-bearing 2,763 Ma Luanga (Machado et al. 1991), which is a polydeformed and metamorphosed stratiform body composed of dunite, harzburgite, orthopyroxenite, and mela- and leuco-norite (Suíta 1988).

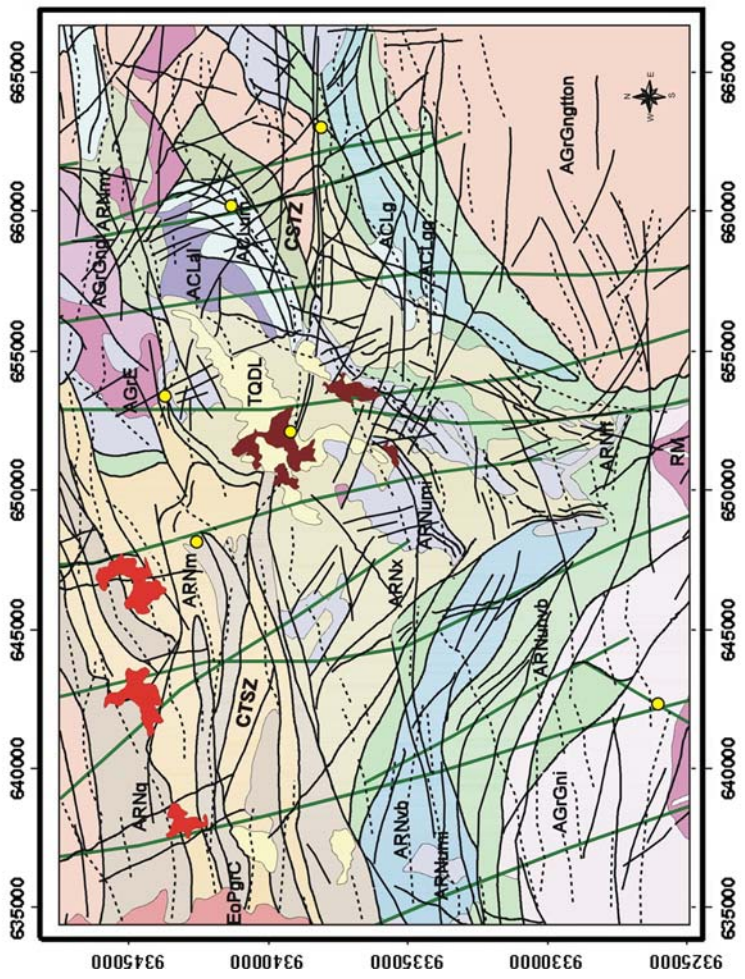
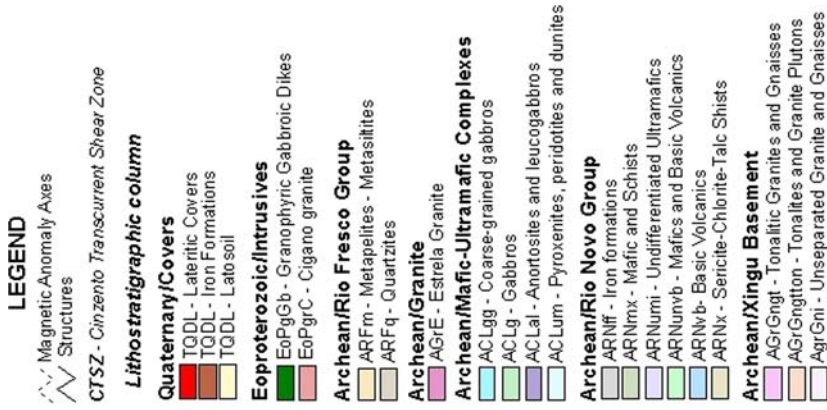


Fig. 2 Geological map of the Serra Leste region (modified from Veneziani and Okida 2001). Yellow circles mark mineral deposits

A NE-elongated belt of the Rio Fresco Group/Águas Claras Formation rests unconformably on the Rio Novo Group (Docegeo 1988). Both units, as well as the Luanga Complex, underwent folding and dynamic metamorphism due to reactivation of the Cinzento strike-slip system (Suita and Nilson 1988). At Serra Leste, the east termination of the Cinzento strike-slip system defines the Serra Pelada Divergent Splay (SPDS; Pinheiro and Holdsworth 1997).

Two distinct episodes of granitoid magmatism are recognized in the Serra Leste area. The oldest is represented by the emplacement of the syntectonic alkaline Estrela Granite Complex ($2,763 \pm 7$ Ma; Barros et al. 2001). The Estrela granite crops out as an EW elongated elliptical body concordant with the regional structures. A contact metamorphic aureole (hornblende and pyroxene hornfels facies) was produced in the meta-volcano-sedimentary envelope (Barros and Barbey 2000). The second episode is represented by the anorogenic Cigano Granite ($1,883 \pm 2$ Ma; Machado et al. 1991), exposed about 15 km west of Serra Pelada Au–Pd–Pt deposit. Dioritic and granodioritic plugs and gabbro dikes of uncertain age also occur in the area.

4 Serra Leste Mineral Deposits

4.1 Luanga Chrome–PGE deposit

The Luanga complex is represented by a meta-ultramafic unit composed of layers of serpentinite, pyroxenite, norite with intercalated chromitite, and by a meta-mafic unit with leucogabbro, anorthosite, and chromitite layers (Nunes 2002).

The igneous minerals of these host rocks were partially replaced by a hydrothermal assemblage of talc, tremolite, serpentine, albite, chlorite, epidote, actinolite, phlogopite, carbonate, tourmaline, orthoclase, and albite in intensely hydrothermally altered areas (Suita et al. 2005). This hydrothermal overprint is structurally-controlled and also resulted in magnetite formation due to the destabilization of olivine from ultramafic rocks. Intensely mylonitized ultramafic rocks within the SPDS are represented by serpentinite with up to 50% of magnetite and chlorite-amphibole-(tremolite-actinolite)-talc mylonites (Nunes 2002).

Sulfides acted as PGE collectors and were likely important to the genesis of the ore. Ore minerals are pentlandite, pyrrhotite, millerite, chalcopyrite, mackinawite, Fe–Ni alloy, braggite, sperrylite, and PGE-bearing sulfo-arsenides (Suita 1988; Diella et al. 1995). The PGE are hosted in three rock types: (i) meta-pyroxenite cumulate layer with intercumulus pyrrhotite and pentlandite; (ii) folded layers of disseminated to massive chromite (1 m-thick and extending for about 1 km), near the contact between mafic and ultramafic units (peridotite/serpentinite); and (iii) chlorite-amphibole-(tremolite-actinolite)-talc mylonite, originated from shearing of the meta-ultramafic rocks (Nunes 2002).

The main mineralization, associated with sulfide-rich levels, is considered ortho-magmatic in origin, as well as the mineralization associated with the chromitite layers. Additionally, the influence of hydrothermal fluids and remobilization associated with mylonitization on the isotopic and geochemical features of the Luanga rocks has also been considered important processes in ore concentration (Suita 1988; Suita et al. 2005; Girardi et al. 2006). This could explain the association of PGE ore with the chlorite-amphibole-(tremolite-actinolite)-talc mylonite.

4.2 Serra Pelada/Serra Leste Au–Pd–Pt deposit

The Serra Pelada Au–Pd–Pt deposit became famous due to a spectacular gold rush in the early 1980s. The deposit is located in the deeply weathered hinge zone of a recumbent syncline. It is hosted by fine-grained carbonaceous meta-siltstone, commonly brecciated and hydrothermalized, close to the contact with dolomitic marble of the Rio Fresco Group/Águas Claras Formation (Tallarico et al. 2000; Moroni et al. 2001). The host rocks are intercepted by dioritic intrusions, which have been affected by chloritization and are crosscut by sulfide-bearing quartz veins (Tallarico et al. 2000).

The orebodies are enveloped by silicified rocks with jasperoid, sericite, tourmaline, kaolinite, chlorite, hematite, chalcopyrite, and carbonate. Primary sulfide minerals are rare within the mineralized zones due to the intense supergene alteration. However, SEM studies led to identification of pyrite, chalcopyrite, arsenopyrite, covellite, bornite, galena, Ni-sulfides (millerite and pentlandite) and Ni–Co–(Cu)-sulfides (carrolite and siegenite; Tallarico et al. 2000).

The near-surface bonanza ore occurs as brecciated, but completely disaggregated, quartz-bearing clayey masses. Supergene oxidation increased gold fineness and grade, developing giant gold nuggets that occur in powdery, earthy material (Tallarico et al. 2000). Platinum group minerals (PGM) occur associated with palladian gold and native palladium and include “guanglinite”, atheneite, isomertieite, sudovikovite, and palladseite (Cabral et al. 2002a, b). According to Cabral et al. (2002a), the Serra Pelada As–Sb–Hg–Se mineral assemblage is typical of hydrothermal vein-type deposits formed at relatively low temperatures.

4.3 Serra Verde Cu–Mo–Au deposit

The Serra Verde Cu–Mo–Au deposit is a small vein deposit with a gold-enriched supergene zone situated in a N30W trending 45°–80°SE dipping brittle fault. It is hosted by the Rio Novo meta-volcanic-sedimentary unit that includes schist, gabbro and meta-mafic volcanic rocks near the contact with the Estrela granite (Marschik et al. 2001, 2005). The host rocks were affected by propylitic alteration and tourmalinization (Villas and Santos 2001). The ore comprises chalcopyrite, pyrrhotite, pyrite, molybdenite, minor magnetite, and gold associated with quartz, amphibole, tourmaline, apatite, and biotite (Villas and Santos 2001). These authors have considered the ore deposition as related to a sub-sea floor event. However, Marschik et al. (2005) obtained a Re–Os age of $2,609 \pm 13$ Ma for molybdenite from Serra Verde, which points to a genetic relationship with 2.56–2.76 Ga alkaline granitoids or 2.6–2.7 Ga volcanic-arc type magmatism.

4.4 Serra Leste iron and manganese deposits

The Serra Leste area also hosts a manganese and an important iron deposit. The latter contributes to the Carajás estimated total iron ore resources of 18 Gt of high-grade (67% Fe) hematite ore (Dalstra and Guedes 2004). At Serra Leste, the iron ore is contained in highly oxidized bodies. The protore is represented by a foliated, folded, and hydrothermalized banded iron-formation unit of the Grão Pará Group (Itacaiúnas Supergroup) and characterized by a low-temperature oxidized hematite-dolomite \pm calcite assemblage. The proposed genetic model for the Carajás iron deposits involves structural-controlled hydrothermal upgrading preceding supergene formation of the economic ores (Dalstra and Guedes 2004; Lobato et al. 2005).

The Sereno manganese deposit is hosted in meta-sedimentary units of the Rio Fresco Group/Águas Claras Formation, near the contact between carbonaceous phyllite and a red bed sequence, represented by meta-sandstone, meta-siltstone and meta-conglomerate with rhodocrosite-bearing phyllite lenses. The ore is associated with a thick clayey horizon and lateritic crusts. It is composed mainly of manganese oxi-hydroxides, such as cryptomelane, todorokite and hollandite, besides pyrolusite, lithiophorite, kaolinite, gibbsite, and goethite.

5 Data Acquisition

The airborne geophysical data was acquired during two distinct surveys. Magnetic and electromagnetic data were obtained by Geotrex-Digheem in March 1999, using a CASA C-212 aircraft. Flight lines were E–W-oriented, perpendicular to the general N–S-trend of the Rio Novo Group rocks, and spaced 250 m. Control flight lines were N–S-oriented and spaced of 5,000 m. Flight height was 120 m above the ground. The height of the electromagnetometer was monitored by a PS100E laser platform, whereas the flight height was monitored by a TRA altimetric radar and a Rosemount 1241M3B1 barometer (Geomag 1993). Gamma-ray spectrometric data was acquired by GEOMAG in June 1993, using a 212 Bell helicopter. The GR-820 Exploranium gamma-ray spectrometric system measured the natural gamma-ray spectrum in 256 channels at a height of 60 m. Its detector consists of four 4" × 4" × 16" thallium-activated NaI crystals, comprising a total volume of 1,024 cubic inches. The sample rate was five readings per second at each 6 m (Geomag 1993). All necessary corrections to the raw data were carried out by GEOMAG and Geotrex-Digheem.

6 Data Processing and Methods

Both radiometric and magnetic data were pre-processed in order to detect and to remove spikes. This was accomplished using a fourth-difference analysis (see, e.g., Blum 1999), in which the value of the radiometric or magnetic field at a given point was replaced by the differences among the values at the four nearest neighbor points along a given flight line. In cases where the fourth difference was found higher than the standard deviation of the data, the magnetic or radiometric value was checked for the presence of positioning or measurement errors.

After spike removal, the data was interpolated using a minimum curvature algorithm (Briggs 1974). The grid cell size was chosen to be 1/5 of the flight line spacing (50 m). With such cell size the spectral content of the original field was almost entirely preserved, whereas the aliasing effect was avoided. The IGRF-1995 (International Geomagnetic Reference Field; IAGA 1996) was removed from the total magnetic field intensity grid in order to separate shallow from deep magnetic sources.

Microlevelling was performed on the grids to remove flight-line related noise, using the method proposed by Minty (1991). The technique was applied using a sequence of filters as follows: (i) a high-pass filter with a cutoff wavelength (λ_c) of the order of twice the flight line spacing to the original grid 'A', along a direction perpendicular (E–W) to the flight line (N–S)—the result was stored in grid 'B'; (ii) a low-pass filter with λ_c of the order of 1 to 3 times the tie spacing to grid 'B', along the flight line direction—the result was stored in a grid 'C', which contained the microlevelling errors. Finally, grid 'C' was subtracted from grid A to produce a microlevelled grid (Fig. 3).

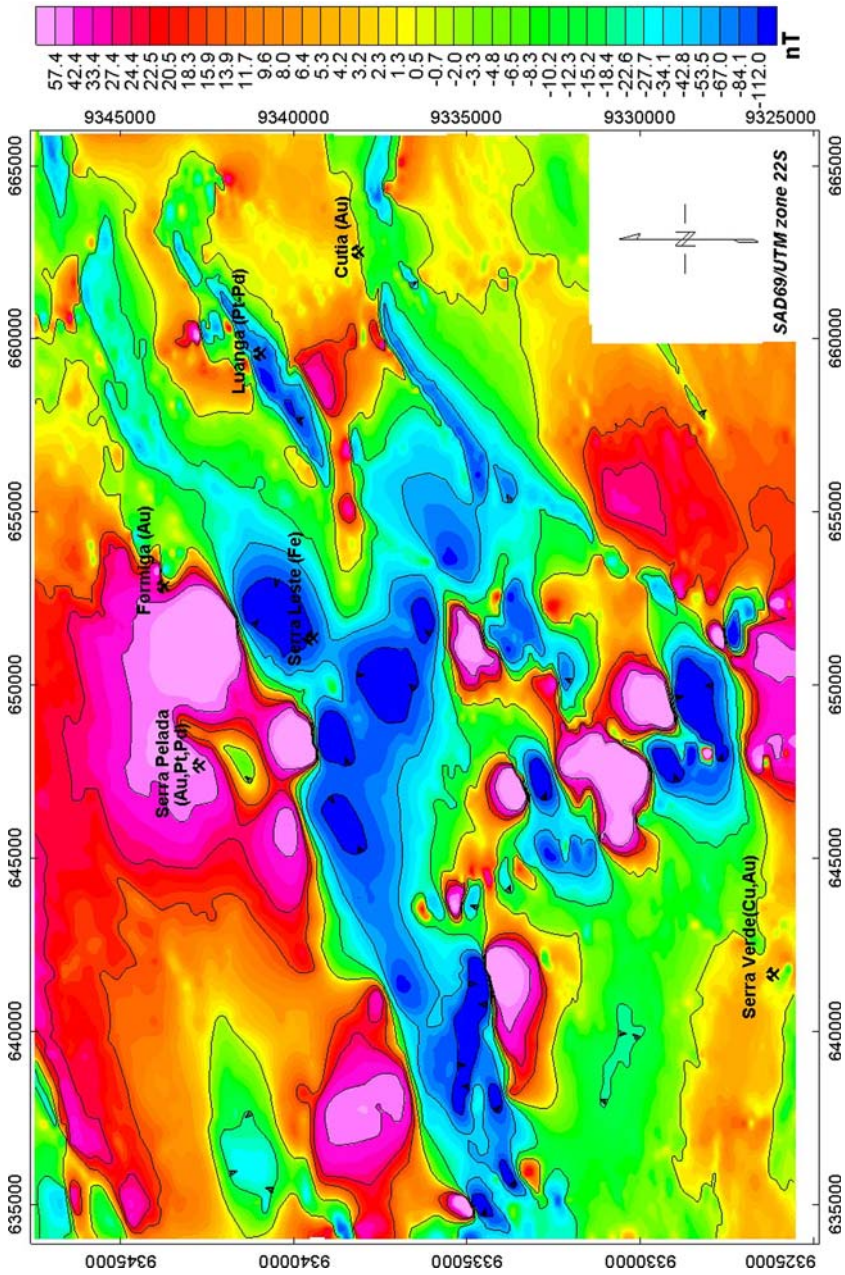


Fig. 3 False-color map of the microleveled anomalous magnetic field. The field was filtered with a 3×3 Hanning filter

The 3D analytic signal amplitude (ASA) (Fig. 4) of the anomalous microlevelled magnetic field (see e.g., Roest et al. 1992; Debeglia and Corpel 1997) was calculated in order to detect edges and boundaries of the anomalous sources based on the premise that, in some special cases, its shape and magnitude may be independent of the geomagnetic inclination and declination and the direction of magnetization sources. When the magnetic latitude is low and the sources of interest are shallow, which is the case here, the ASA has the property to have their maxima directly over the anomalous sources (Hsu et al. 1996; Huang et al. 1997; Huang and Guan 1998; Li 2006).

Complementary to the ASA (Fig. 4), the ratio between the vertical and horizontal gradients of the magnetic field, i.e. the analytic signal phase (ASP; Thurston and Smith 1997) (Fig. 5), as well as the horizontal gradient amplitude (HGA) (Fig. 6), were calculated with the aim of mapping structures and lineaments (see e.g. Cordell and Grauch 1985; Milligan and Gunn 1997). The horizontal gradients were calculated in the space domain by a 9×9 convolution filter, whereas the vertical gradient was calculated in the frequency domain by multiplying its spectrum by an appropriate factor and then converting the result to the space domain through an inverse Fourier transformation (Gunn 1975; Geosoft 2006).

The 3D Euler deconvolution was applied to estimate depths to the magnetic anomalous sources (Reid et al. 1990; Hsu 2002). In this method, depths and horizontal positions are calculated by solving linear systems of Euler's homogeneity equations (Thompson 1982), where the knowing parameters are: (i) an anomalous magnetic field; (ii) its gradients along the $-x$, $-y$ and $-z$ directions; and (iii) a structural index (SI), which is a parameter that provides information about the geometry of the anomalous sources. Solutions were obtained for SI equal to 0.5, 1, 2 and 3. A 20×20 window was chosen to estimate each solution associated to each grid cell based on the mean size of the magnetic anomalies of the study area. Since the grid spacing is 50 m, the window size is 1,000 m, meaning that anomalies with wavelengths longer than this value are not well represented and unreliable depth estimates may occur. Solutions were accepted if the following two criteria were satisfied: (i) the uncertainty in the depth estimate is less than 10% of the calculated depth; and (ii) the distance from the center of the window to the source is less than 500 m. These two criteria were used to restrict solutions in terms of both vertical and horizontal positions, because the primary goal here is to retain only statistically good estimates of depths.

7 Magnetic Interpretation

Magnetic field anomalies (Fig. 3) highlight the structural framework and main geological features in the study area. Field derivatives further highlighted detailed features. High values of the Amplitude of the Analytic Signal (ASA; Fig. 4) are associated with meta-ultramafic rocks of the mafic–ultramafic complexes and magnetite-rich shear zones related with the Serra Pelada Divergent Splay (SPDS; Pinheiro and Holdsworth 1997). Anastomosed ductile shear zones form the axes of the anomalies in the phase of the analytic signal map (ASP; Fig. 5). High frequency anomalies in the analytic signal map (Fig. 4) can be seen in the central part of the study area. These anomalies are associated with small and shallow magnetic sources.

Magnetite-rich, sub-parallel splays related to the Cinzento Transcurrent Shear Zone (CTSZ) cross-cut the Luanga complex. NE-oriented anomalies over this complex observed in the horizontal magnetic field gradient map (Fig. 6) show that such magnetite content may be the source of the magnetic anomalies. N–S oriented discrete features are associated with grabbroic dikes of unknown age.

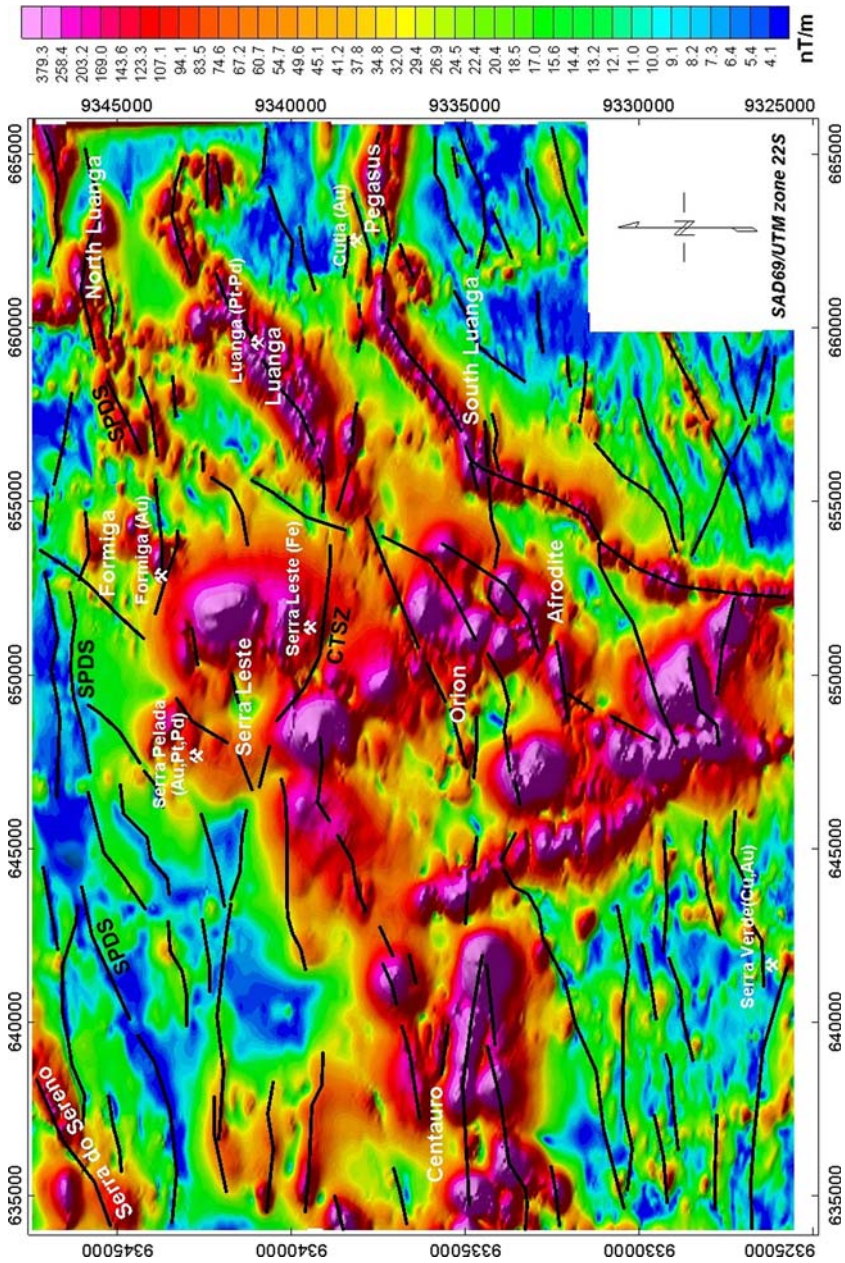


Fig. 4 False-color map of the amplitude of the anomalous magnetic field analytic signal. CTSZ, Cinzenzo Transcurrent Shear Zone; SPDS, Serra Pelada Divergent Splay

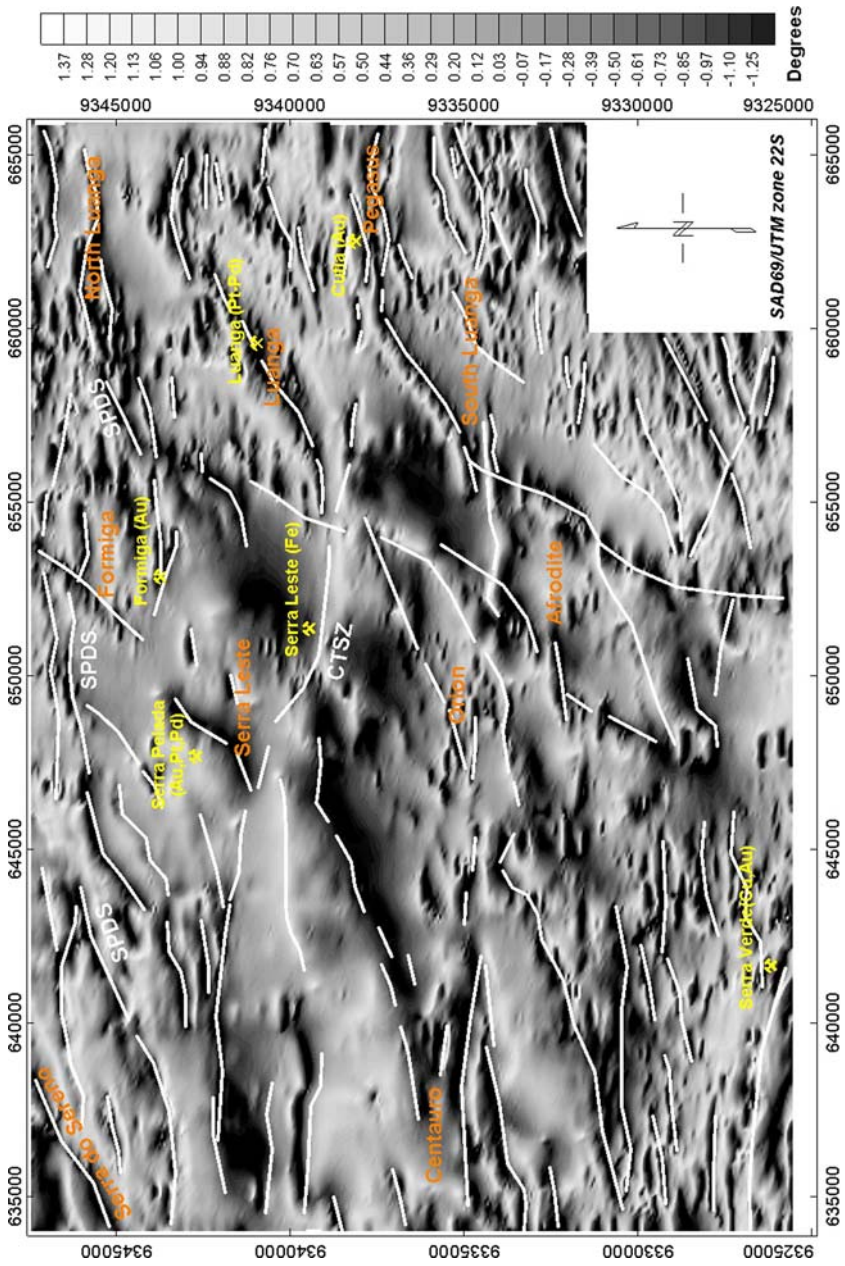


Fig. 5 Gray-shaded map of the phase of the anomalous magnetic field analytic signal. Given names on the map refer to meta-mafic and meta-ultramafic units and the Cinzenito Transcurrent Shear Zone (CTSZ)

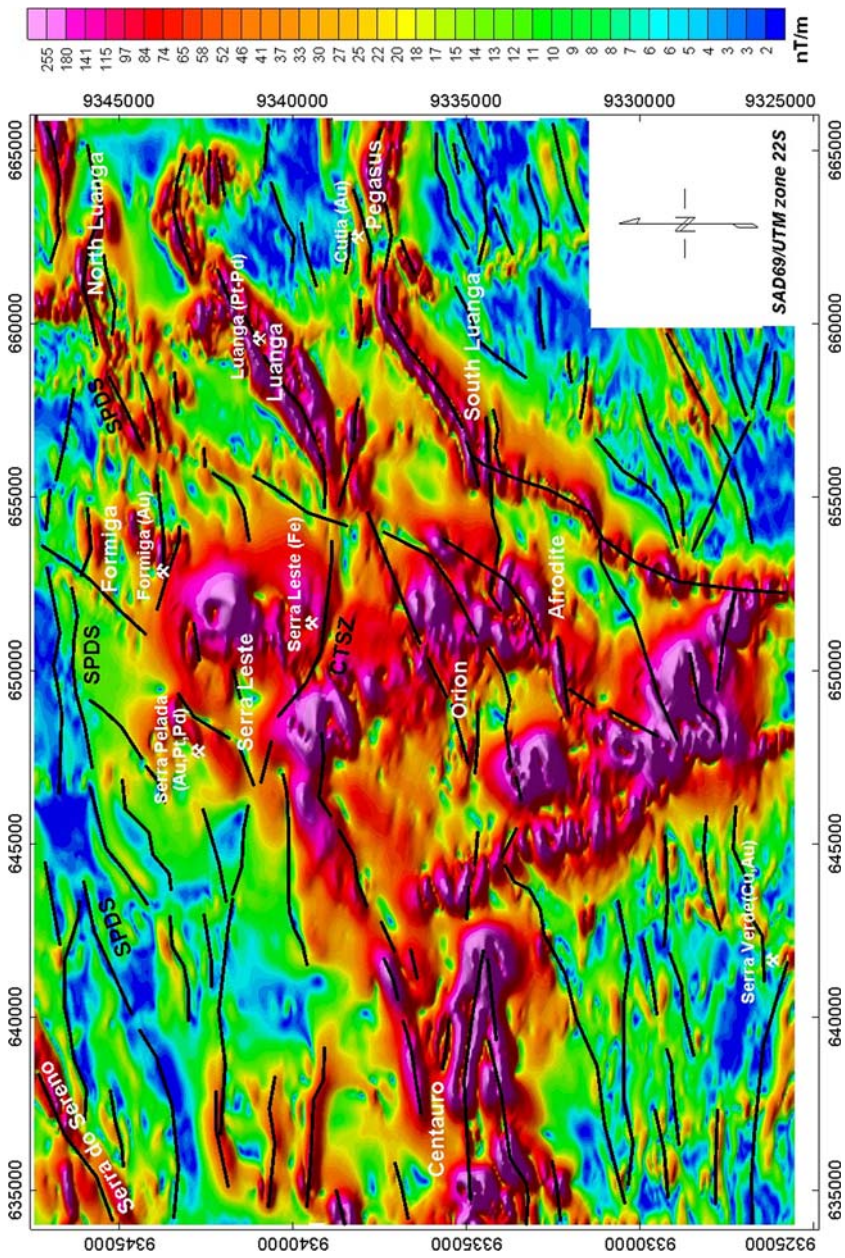


Fig. 6 False-color map of the horizontal gradient of the anomalous magnetic field. CTSZ, Cinzento Transcurrent Shear Zone; SPDS, Serra Pelada Divergent Splay

High values of the ASA (Fig. 4) and the ASP axes over the mafic–ultramafic complexes are associated with magnetite-enriched meta-ultramafic rocks, such as dunite, peridotite, serpentinite, and talc-schist, as well as shear zones that truncate these complexes and remobilized the magnetite from the meta-ultramafic units. High values of the ASA (Fig. 4) also occur in the central-north portion of the study area, reflecting the presence of banded iron formations. Discontinuities in the high values of the NS or NNW anomaly patterns likely represent magnetite-enriched gabbroic dikes, which are widespread in the Itacaiúnas Supergroup. A high-value ASA anomaly (Fig. 4) in the NW portion of the study area reflects the Serra do Sereno meta-sedimentary rocks that contains Mn mineralizations. The geometry and spatial displacement of the mafic–ultramafic Luanga and south Luanga complexes shown in the ASA map (Fig. 4) indicate ductile shearing with a dextral sense, with sinistral shearing reactivation. The ASP map (Fig. 5) highlights lineament axes that are not so evident in the ASA map (Fig. 4), mainly those associated with the CTSZ second-order structures, as described in Siqueira (1996) and Pinheiro and Holdsworth (1997). Whereas in the ASA map (Fig. 4) it is possible to observe the NS oriented gabbroic dikes, the ASP (Fig. 4) highlights mainly the EW oriented features associated with transcurrent shear zones of the Serra Pelada Divergent Splay.

Figure 7a–d shows Euler deconvolution maps superposed to the geological map of Veneziani and Okida (2001). The main statistical parameters of the solutions are presented in Table 1. The correct Structural Index (SI) for a given feature was estimated as that which gave the tightest clustering of solutions (Reid et al. 1990). Good clustering of solutions were obtained using $SI = 0.5$ (Fig. 7a) and $SI = 1$ (Fig. 7b) for most of the features in the study area. However, distinctions between the two maps can be made for some features. For example, NE–SW-trending linear features within the Xingu basement on the east of the Serra Verde (Cu, Au) deposit and a E–W-trending feature underneath the central-north portion of the study area, crossing the boundary between the lateritic covers and Archean schists on the west of the Serra Leste (Fe) deposit, are better enhanced with a $SI = 0.5$ (Fig. 7a). Linear NE–SW trends associated to mafic–ultramafic complexes on the northeast of the study area and to Archean rocks on the northwest are best displayed with $SI = 1.0$ (Fig. 7b). There is also a linear NE–SW trend that is clearly seen with $SI = 1.0$ (Fig. 7b) near the Luanga chrome–PGE deposit. Most of the depths for the best solutions using $SI = 0.5$ (Fig. 7a) and $SI = 1.0$ (Fig. 7b) are in the range of 100–300 m. These features are likely to be near vertical contacts and faults with moderate throws ($SI = 0.5$; Fig. 7a) and faults with small throws ($SI = 1.0$; Fig. 7b). Figure 7c ($SI = 2$) suggests that narrow, vertical pipes can be associated to some mineral deposits in the study area. The most interesting features represented by good clustering of solutions in this map are the curved trends underneath the lateritic covers surrounding the Serra Leste Fe deposit, with depths ranging from 600 to 1,000 m, and the linear NE–SW trend within Archean rocks surrounding the Serra Pelada Au–Pt–Pd deposit, with depths spanning from 400 to 700 m. Less reliable solutions are exclusively obtained with $SI = 3$ (Fig. 7d), suggesting that geological features that can be approximated to relatively small magnetized spheres are probably inexistent in the study area, with the exception of few areas on the east portion where good clustering was obtained with depths ranging from 400 to 500 m near the Cutia (Au) deposit and 100 to 300 m near the Luanga chromium–PGE deposit.

8 Radiometric Interpretation

Low values of total gamma radiation count (Fig. 8) are associated with outcrops of the mafic–ultramafic complexes. Areas with high values can be related to the presence of Archean granitic

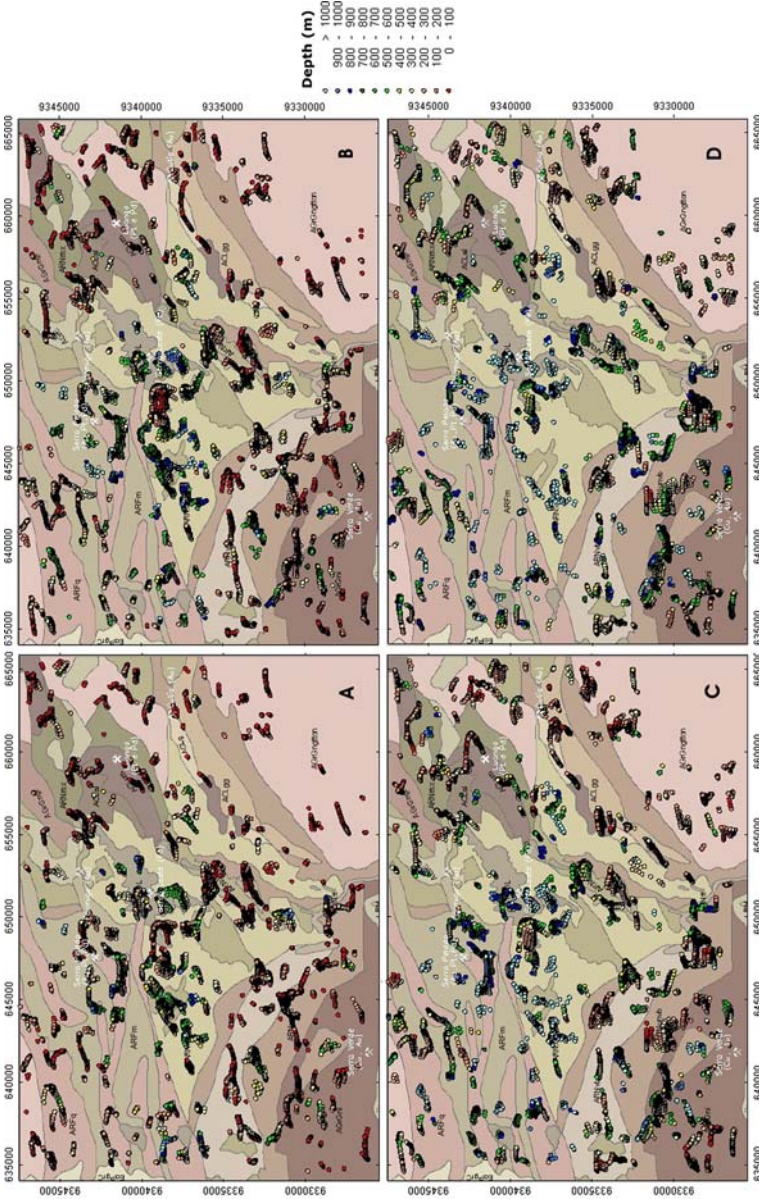


Fig. 7 Euler solutions obtained using a 20×20 window and an acceptance level of 10% for different structural indexes (SI). (a) SI = 1; (b) SI = 1; (c) SI = 2; (d) SI = 3. Lithologies (Veneziani and Okida, 2001): (EoPgCb) granophyric gabbroic dikes; (ACLum) pyroxenite, peridotite and dunite; (ACLgg) coarse-grained gabbro; (ACLg) gabbro; (ACLal) anortosite and leucogabbro; (AgrE) Estrela Granite; (ARNx) sericite-chlorite-talc schist; (ARNvb) basic volcanic rocks; (ARNumb) mafic and basic volcanics; (ARNum) undifferentiated ultramafic rocks; (ARNmx) mafic rocks and schists; (ARNxt) tonalitic granite and gnaiss; (AgrGngt) tonalite and granite plutons; (AgrGnt) unseparated granite and gnaiss; (ARFq) quartzite; (ARFm) meta-pelite and meta-siltite

Table 1 Statistical parameters related to depths estimated by Euler deconvolution method

Si	Number of solutions	Depth (m)		
		Minimum	Maximum	Mean
0.5	12,536	0	1,622	242 ± 6
1.0	14,112	0	1,966	287 ± 5
2.0	13,115	13	1,990	423 ± 5
3.0	10,753	84	1,998	558 ± 5

SI stands for Structural Index

rocks of the Estrela Granite Complex (AgrE), the Xingu Complex (AgrGni and AgrGntton) and Paleoproterozoic Cigano-type granites (EoPgrC). Intermediate to high values in the central area reflects the sericite-rich quartzite and schist of the Rio Fresco Group (ARFq).

The Thorium color map (Fig. 9) shows a positive correlation between low values and spatial positions of meta-mafic–ultramafic rocks. High values in this map represent Archean granitic rocks of the Xingu Complex (AgrGni and AgrGntton), the Estrela and the Cigano granites, the Rio Fresco Group meta-sedimentary rocks (ARFq and ARFm) and lateritic regoliths (TQDL). The position of the mafic–ultramafic Luanga and south Luanga complexes indicates sinistral sense of shearing along the CTSZ.

The RGB ternary map of K, U and Th channels (Fig. 10) provides additional information when compared to individual channel maps (e. g. Dickson and Scott 1997; Gunn et al. 1997). Low Th values associated with mafic–ultramafic complexes also appear as low values in the ternary map (dark colours). It is also possible to detect areas of predominant K (red tones), which indicates an enrichment in this element. Red tones over the Luanga complex reflect granite outcrops of the Estrela granite (AgrE) and hydrothermal alteration associated with granite intrusions. Light blue and yellow coloured areas represent the Estrela granite in the Formiga deposit area. The Cigano granite (EoPgrC) appears in light blue tones and white coloured areas, indicating a relative predominance of U content; although it shows high absolute values for the three channels. Greenish areas in the ternary map represent Th-enriched lateritic and quaternary covers (TQDL). Blue coloured areas in the Serra Leste iron deposit lies exactly where CTSZ truncates the plateau and where iron formation outcrops occur. This characteristic indicates a predominance of U content in the CTSZ surrounding area. This may indicate that a change in chemical conditions led to enrichment in this radiometric element, as similarly observed by Dickson and Scott (1997) in the southeast of Australia. Such enrichment can be interpreted as evidence for hydrothermal alteration.

In general, the discontinuities seen in the radiometric maps represent steep contacts between large lithological domains, suggesting tectonic fault-controlled blocks and shear zones along contacts.

8.1 Time Domain Electromagnetic Interpretation (TDEM) Interpretation

The apparent conductance map (Fig. 11) shows main conductive zones in: (a) the NE portion of the map, where there are NE-trending aligned features (part of Sereno Hill), which may represent carbonate and manganese-rich phyllite of the Rio Fresco Group; (b) the surroundings of the Formiga deposit, highlighting the thick alteration mantle, the meta-ultramafic rocks of the Formiga complex as well as banded magnetite-rich formations; (c) the mafic–ultramafic Luanga complex, represented by meta-ultramafic unit composed of magnetite-rich rocks (dunite, peridotite, and serpentinite), whose crystals are connected by venulation and shear bands; (d) the Serra Pelada Au–Pd–Pt deposit, where high conductive zones occurs due to the

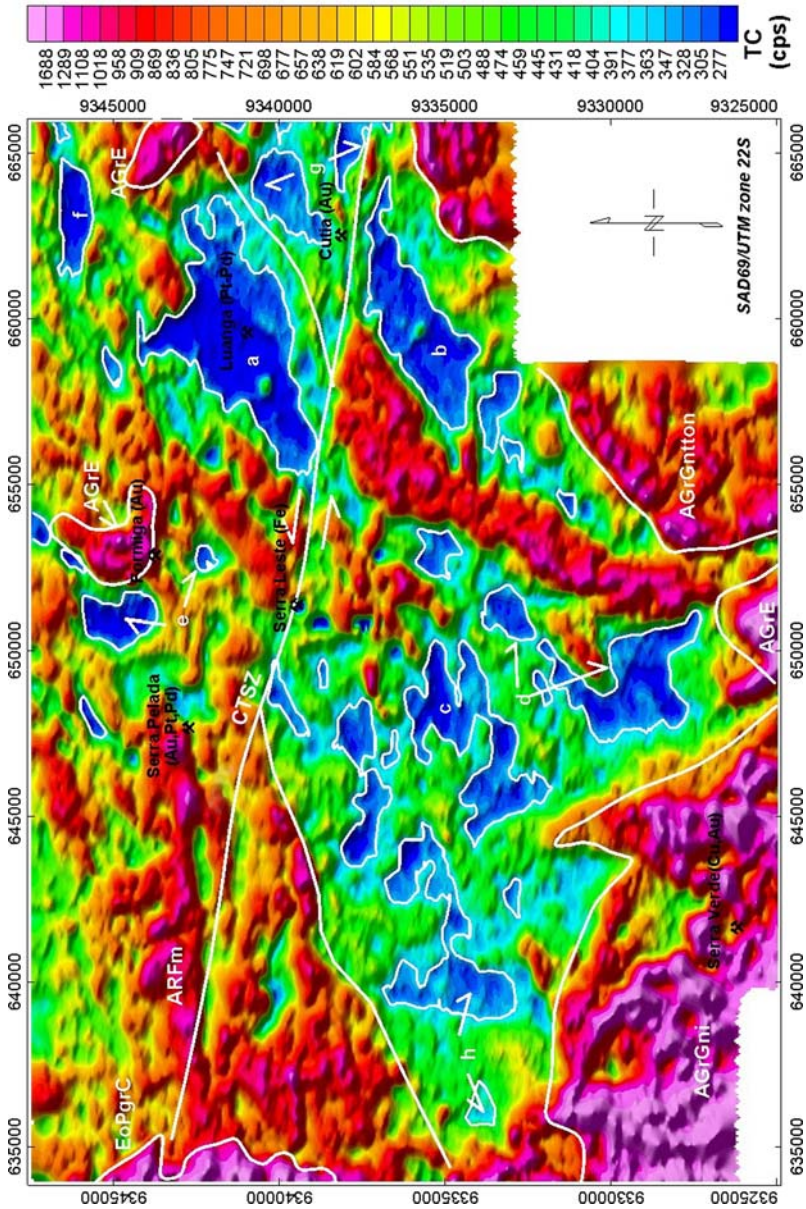


Fig. 8 False-color map of total gamma radiation count (cps). Mafic and ultramafic Complexes: (a) Luanga; (b) Luanga Sui; (c) Orion; (d) Afrodite; (e) Formiga; (f) North Luanga; (g) Pegasus; and (h) Centauro. Lithological units: (AGrGnt e AGrGnton) Xingu Complex; (AGrE) Estrela Granite; (ARFq) sericitic-rich quartzite of the Rio Fresco Group; (EoPgrC) Cigano Granite. The Cuzco Transcurrent Shear Zone (CTSZ) is also shown on the map

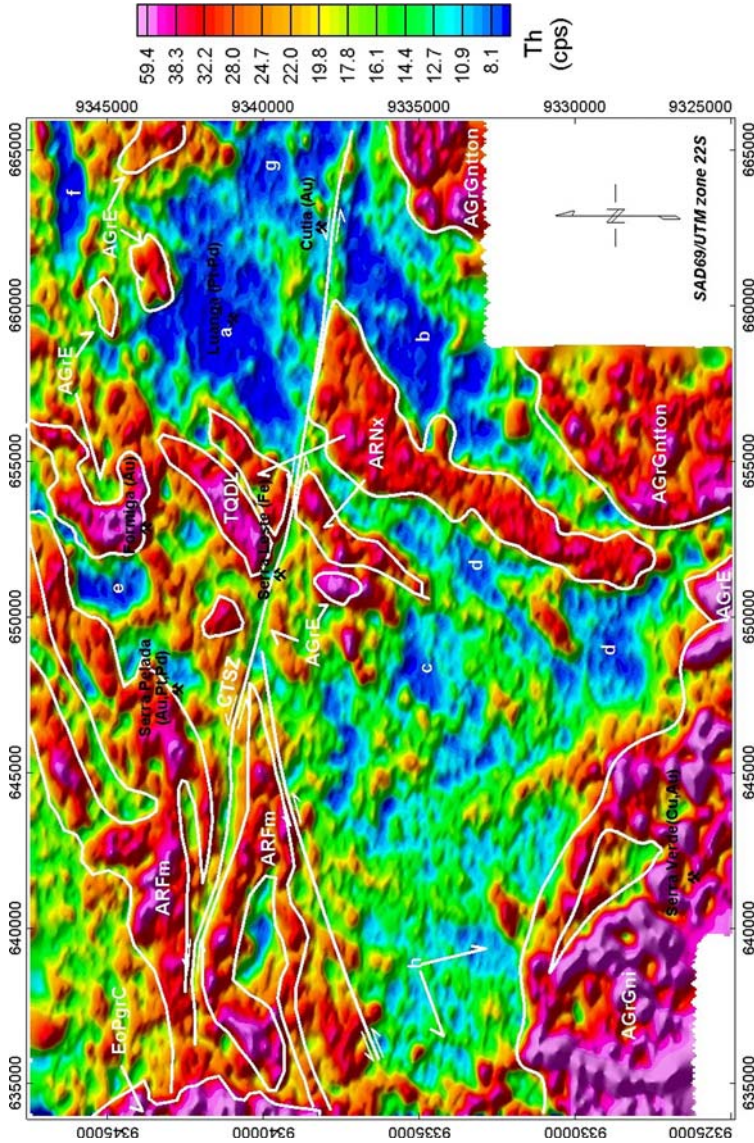


Fig. 9 False-color map of Thorium radiometric count (cps). Mafic–ultramafic Complexes: (a) Luanga; (b) Luanga Sul; (c) Órion; (d) Afrodite; (e) Formiga; (f) Luanga Norte; (g) Pegasus; and (h) Centauro. Lithological units: Iron Formations (TQDL); Xingu Complex (AGrGni e AGrGnton); Estrela Granite (AGrE); sericite-rich quartzite of the Rio Fresco Group (ARFq); meta-pelite and meta-siltite of the Rio Fresco Group (ARFm); and Cigano Granite (EoPgrC). The Cinzenzo Transcurrent Shear Zone (CTSZ) is also shown on the map

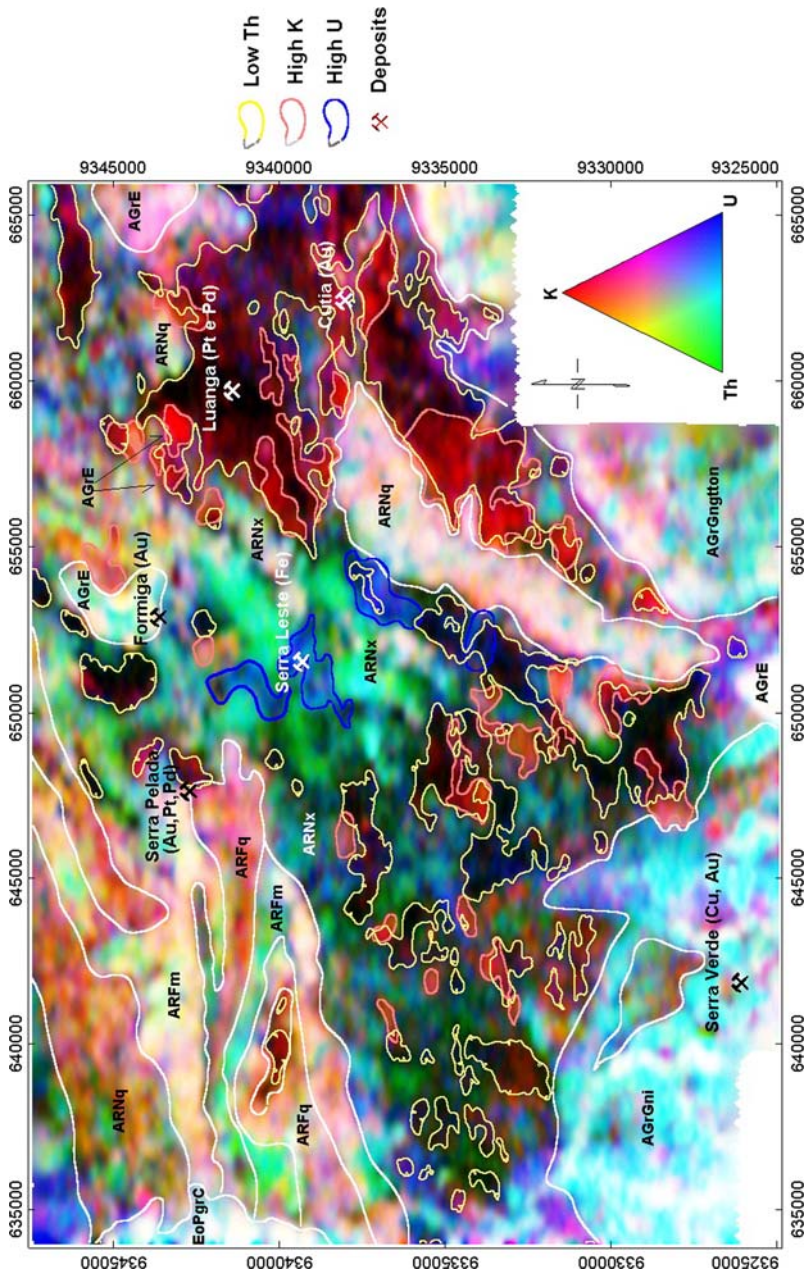


Fig. 10 Radiometric ternary map (Red: K, Green: Th; Blue: U). Lithological units: Xingu Complex (AGrGni e AGrGntton); Estrela Granite (AGrE); Cigano Granite (EoPgrC); sericite-rich quartzite of the Rio Fresco Group; (ARFq); meta-pelite and meta-siltite of the Rio Fresco Group (ARFm); and sericite-chlorite-talc schist (ARNx)

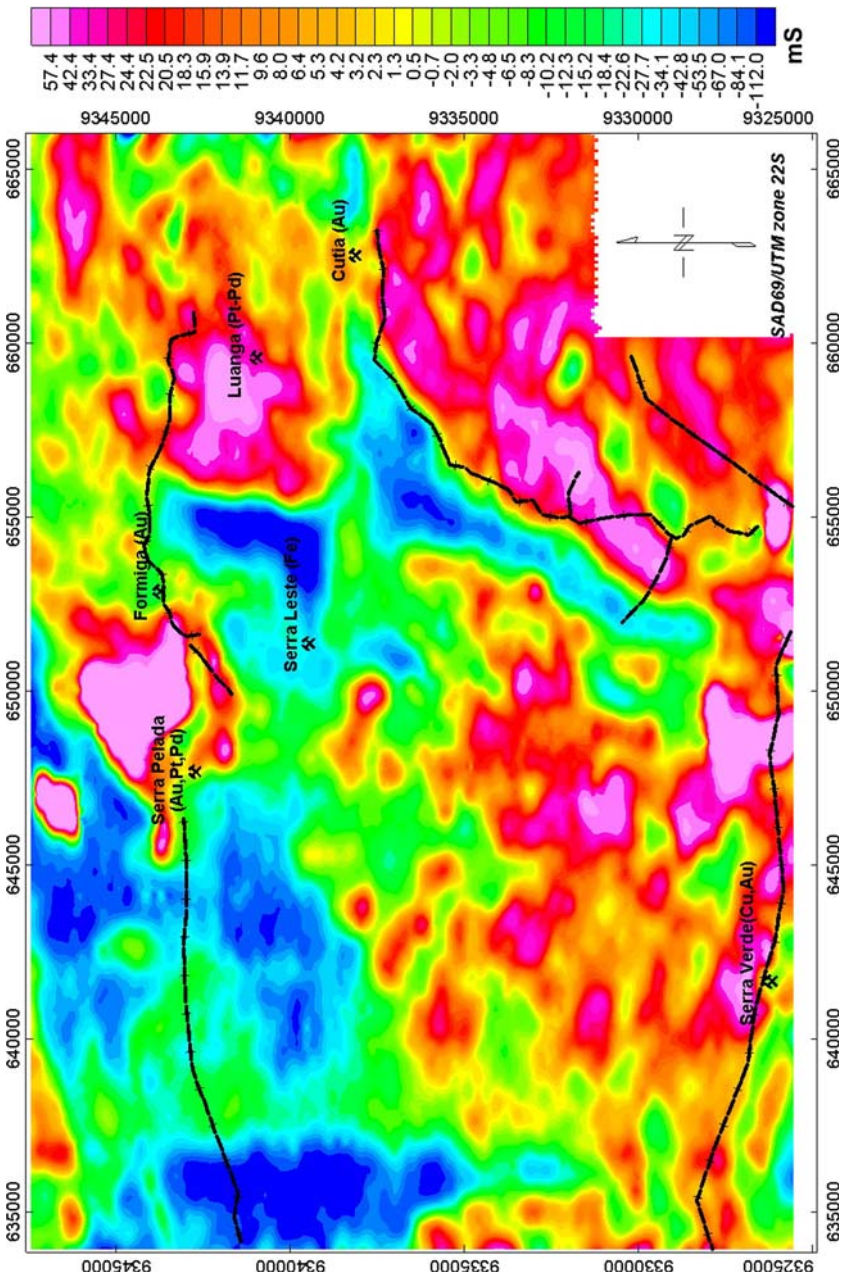


Fig. 11 False-color map of apparent conductance (mS \times 1,000). Given names on the map refer to mineral deposits

presence of carbonaceous meta-siltite and to the thick alteration mantle generated by dissolution of the carbonate-rich meta-sandstone of the Rio Fresco Group.

9 Results

9.1 Integrated Interpretation of Geophysical Maps and Geophysical Signatures of PGE, Au-PGE and Cu–Au Deposits in the Serra Leste Region

High values observed in the ASA map (Fig. 4) represent meta-ultramafic rocks, which comprise the sum of the magnetic responses of dunite, meta-peridotite, serpentinite, sulphide-rich zones with pyrrhotite, and shear zones with magnetite. Formation of magnetite in meta-peridotite occurs simultaneously with talc and serpentine as a product of olivine alteration, and could have been accompanied by PGE remobilization within the shear zones. In the ASP map (Fig. 4), the axes of the anomalies appear as anastomosed features that are ductile shear zones. PGE mineralization in the mafic–ultramafic Luanga complex is also associated with pyrrhotite-rich meta-pyroxenite and chromitite layers next to the contact between meta-pyroxenite and peridotite/serpentinite. Thus, the boundaries of the ASA (Fig. 4) anomalies are likely to be correlated to PGE mineralization.

Mafic–ultramafic complexes show low radiometric values in Figs. 8 and 9. It appears as dark colours in the ternary map (Fig. 10). It is interesting to note that near the Serra Pelada Au–PGE deposit there is a small dark area of low Th values that is compatible with the radiometric signature of meta-mafic–ultramafic units. High ASA values (Fig. 4) and high apparent conductance values (Fig. 11) are also evident and compatible with the signature of these lithologies. A red-shaded zone around Serra Pelada indicates a relative K-enrichment. Such response is associated with hydrothermal activity possibly related to ore deposition. The presence of meta-mafic and meta-ultramafic rocks near this mineralization can be seen as evidence for the source of Pt and Pd associated with Au in the Serra Pelada deposit.

Electromagnetic data shows good correlation with layered mafic–ultramafic complexes, which can be characterized as conductive domains, represented by high apparent conductance values and intermediate values observed on the Conductive Thickness Product (CTP). Electromagnetic data also allows the delimitation of areas with potential to host PGE mineralization in the area.

The Serra Verde Cu–Au–Mo deposit in the southeast portion of the study area contains no magnetite associated with the ore assemblage. Small percentage of pyrrhotite occurrences (<1%) is the source of a discrete ASA anomaly around the Serra Verde deposit (Fig. 4). Red polygons in the ternary map (Fig. 10) indicate K enriched areas, which may reflect hydrothermal alteration. These areas are probably related to granitic intrusions. Blue polygons include areas with relative U enrichment, which is indicative of hydrothermally altered areas. Such evidences suggest an excellent potential for Cu–Au-mineralization occurrences in these areas. The Serra Verde deposit is also located on a conductive zone that has CTP solutions varying from 11 to 30 milliSiemens. This zone is associated with sulfide veins (chalcopyrite > pyrite > pyrrhotite > pentlandite and cobaltite), quartz and chlorite, embedded in acid volcanic rocks with albite and biotite.

Table 2 shows the geophysical signatures associated with PGE and Cu–Au deposits in the Serra Leste region.

Table 2 Geophysical signatures of Cr-PGE, Au-PGE and Cu–Au–Mo deposits in the Serra Leste region

Deposit	Signature		
	ASA	Gamma radiation	TDEM
Luanga (Cr-PGE deposits)	High	Low total count and Th	High
Serra Pelada (Au-PGE deposit)	High	High K and low Th	High
Serra Verde (Cu–Au–Mo deposit)	Low	High K and U	Discrete conductive anomaly

9.2 Prospective Model for the PGE in the Serra Leste Region

The layered mafic–ultramafic Luanga complex crops out in the form of a NE-striking wedge with its south extremity curved to SW, indicating dextral sense of shearing along the CTSZ. The Luanga complex is represented by a meta-ultramafic unit overlain by a meta-mafic unit. Rocks from the lower meta-ultramafic unit contain abundant magnetite formed as a result of the destabilization of olivine. Igneous layering plunges about 50° to the SE in the south portion of the complex and about 70° to east in the north portion, where layers have NNW orientation. The inverted stratigraphy observed at Luanga is probably due to oblique shearing associated with the CTSZ that took place during the regional deformation.

The hypotheses used to perform airborne geophysical data integration are:

- (i) Low Th values (<10 cps; Fig. 9) are related to occurrences of meta-mafic and meta-ultramafic rocks that host PGE primary mineralization;
- (ii) ASA (Fig. 4) and ASP (Fig. 5) anomalies are due to large magnetite content of the meta-mafic and meta-ultramafic rocks.

A favorability map for PGE mineralization was tailored using the Arc Spatial Data Modeler (ArcSDM—Sawatzky et al. 2007).

The first step to generate the model was to map areas with less than 10 cps in the Th radiometric channel that represent outcrops of mafic–ultramafic complexes. The next step was to draw on the map the interpreted ASA (Fig. 4) and ASP (Fig. 5) anomalies axes that represent magnetite-enriched meta-ultramafic rocks and shear zones with magnetite and PGE ore remobilized from the meta-ultramafic rocks. Three buffers were created around ASA (Fig. 4) and ASP (Fig. 5) anomalies axes. These buffers represent, exclusively, meta-ultramafic units and shear zones that truncate meta-ultramafic rocks. Each buffer is 200 m wide, which delineates areas of 600 m around the axes (Fig. 12). The final step was to produce a map of spatial intersection between buffer areas around the magnetic anomalies axes and low Th cps areas.

Sectors classified as “priority 1” for PGE prospecting in the model comprise areas with meta-ultramafic rock occurrences that are cross-cut by shear zones, similar to the Luanga complex area that hosts the main PGE deposits. Sectors designated “priority 2” contain meta-mafic units with minor PGE mineralization.

Figure 13 displays an area of 53.23 km² favorable for PGE mineralization in the Serra Leste region, which comprises 7.43% of the total study area (716 km²). Thus, the model restricts the area for detailed follow-up work, such as geochemistry surveys and ground geophysics.

10 Discussion

The high-resolution airborne geophysical data employed in this study allowed a synoptic vision of the spatial distribution of the lithological units and tectonic structures of the Serra

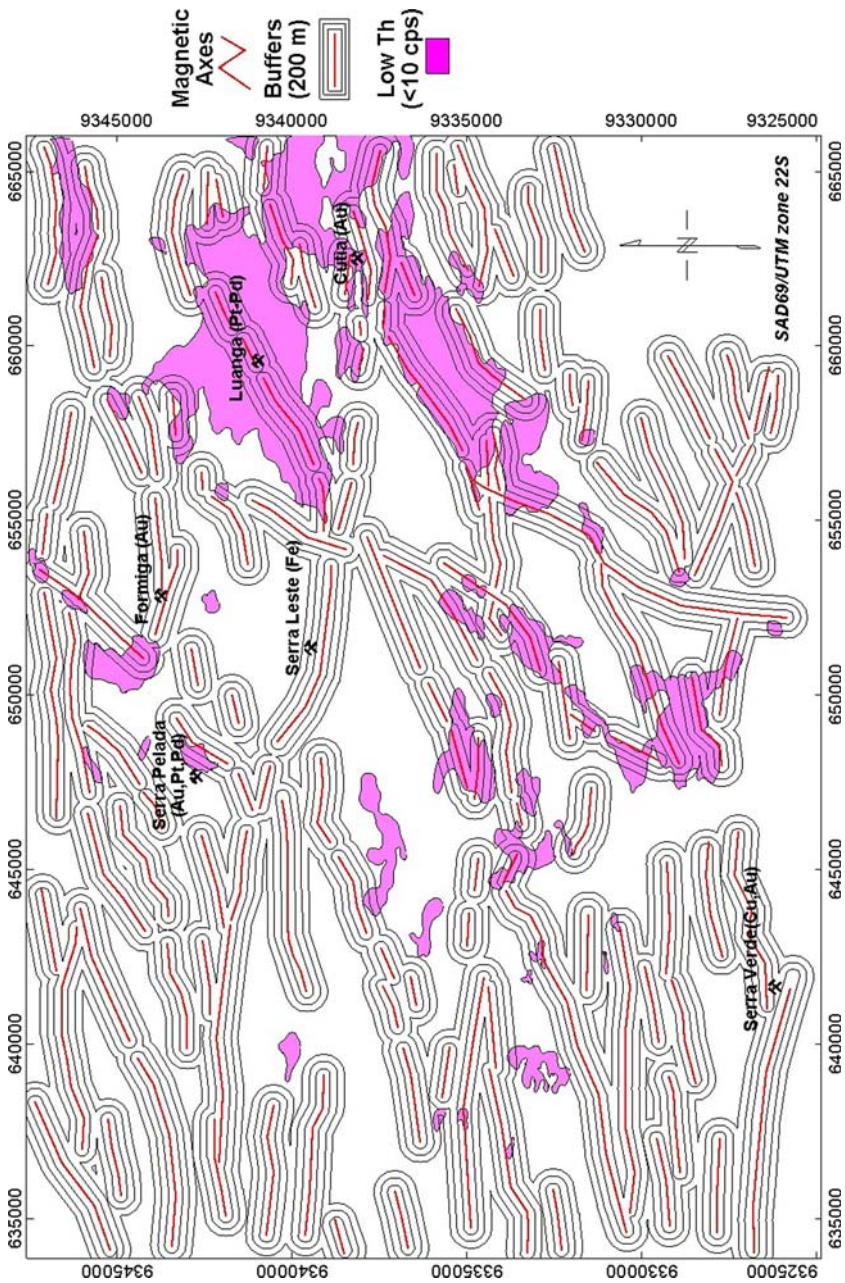


Fig. 12 Buffers around axes of anomalies interpreted from the amplitude and phase of the anomalous magnetic field analytic signal

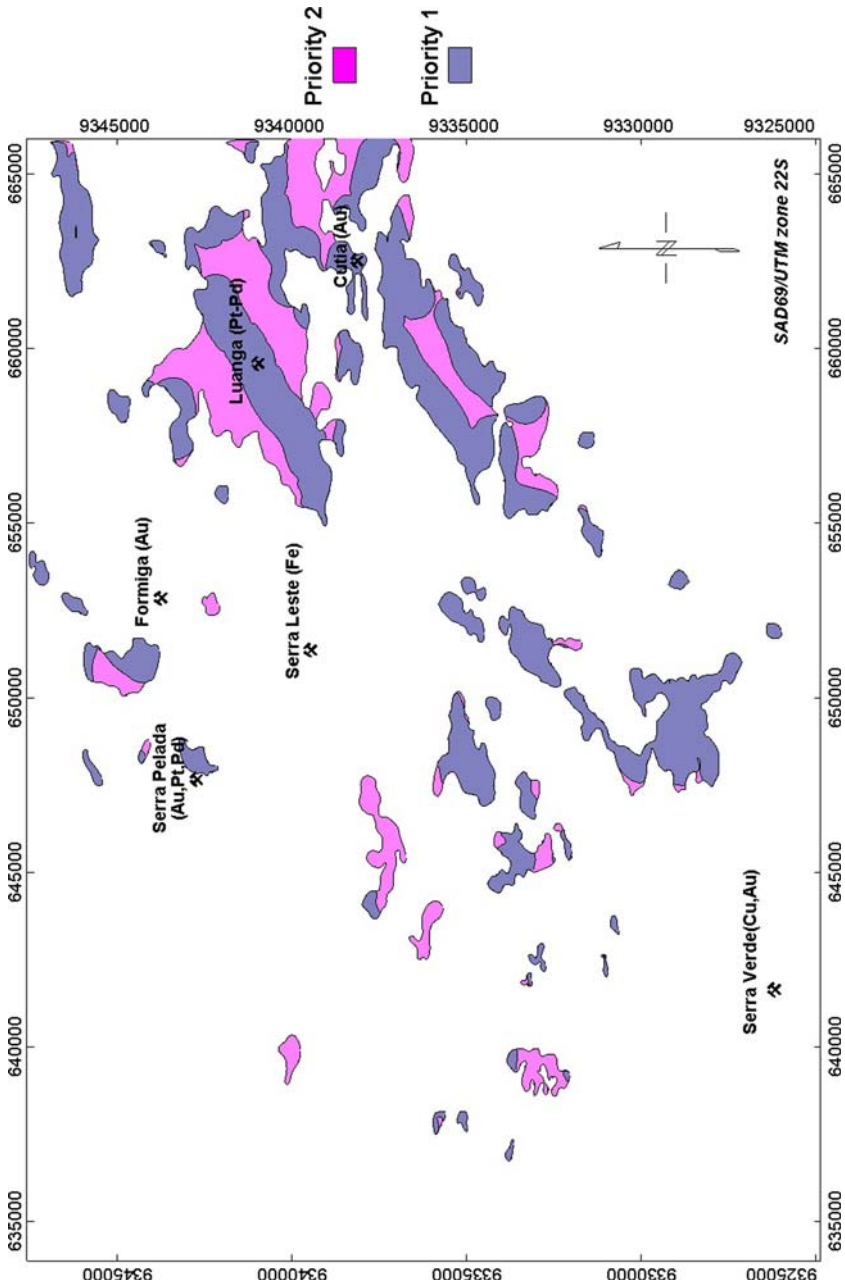


Fig. 13 Mineral potential map for PGE deposits in the Serra Leste region, Carajás Mineral Province (CMP), Brazil

Leste region. The bi-direction gridding of the magnetic data suppressed most of the NNW-trending anomalies related to the magnetite-bearing Neoproterozoic gabbroic dikes, which are almost parallel to the flight lines. In contrast, the minimum curvature gridding proved to be a superior interpolation method as it was able to preserve these anomalies. Microlevelling correction filtered spurious geophysical data along flight lines.

The ASA (Fig. 4) and the ASP (Fig. 5) proved efficient in mapping tabular bodies with steep dips (layers and dikes), which were not verified using the vertical derivative and the horizontal gradient (Fig. 6). The ASA map (Fig. 4) provided mapping of some of the large lithostratigraphic units in the study area, such as layered mafic–ultramafic complexes, gabbroic dikes and some iron formations. Geophysical sub-domains revealed within lithological units, allowed the identification of meta-peridotite and serpentinite layers in the layered mafic–ultramafic complexes. The ASA and ASP maps (Figs. 4, 5) also allowed the cartography of structures such as faults and shear zones.

The Euler solutions provided information about the distribution of magnetic sources under the study area. Using this technique, it is a common practice to employ a window size of 10×10 cells. However, in the case of this work, numerous magnetic anomalies seen in Fig. 3 have wavelengths longer than 500 m, which would encompass a 10×10 window given a grid cell size of 50 m. Therefore, several reliable solutions associated to longer wavelengths would not be obtained. Using a window size of 20×20 grid cells, the method allowed inferring about the geological models associated with the magnetic anomalous sources for most of the solutions. It was shown that several magnetic anomalies of the study area are due to shallow sources (0–500 m depth). The lack of reliable solutions seen in Fig. 7a–d in some portions of the study area is due to near-zero magnetic anomalies or interference of neighboring anomalies.

Archean basement rocks of ages older than 2.9 Ga show high total gamma radiation counts. Rocks of the Estrela and Cigano granites (2.76 and 1.88 Ga, respectively) are identified in the ternary map (Fig. 10) due to the relative K enrichment. Anorogenic granites (1.88 Ga) are characterized by equivalent high values of K, U and Th.

Electromagnetic data indicates the presence of a series of conductive bodies distributed through the study area. These conductors are related to the presence of metal concentrations of various sources. Electromagnetic systems has been a useful tool to identify massive sulfides, iron and manganese formations, among others conductors bodies. However, one must be very careful when interpreting electromagnetic data such as GEOTEM for purposes of identifying superficial targets, because conductive anomalies may also eventually reflect deep conductive structures (Gingerich and Schaefer 1998).

11 Conclusions

Methods on airborne geophysical data processing, interpretation and spatial modeling experimented in this work allowed:

- (i) to delineate magnetite-rich tracts in meta-ultramafic rocks (dunite, peridotite, and serpentinite) and shear zones through ASA (Fig. 4) and ASP (Fig. 5) maps;
- (ii) to estimate depths to magnetic sources (Fig. 7a–d), as well as to infer about their geometry and spatial distribution, by performing 3D Euler deconvolution of the anomalous magnetic field. The results suggest that most of the magnetic anomalies are due to shallow (0–500 m depth) near vertical faults and irregular or curved near vertical contacts or dikes. Relatively deep (500 to more than 1,000 m depth) vertical

- pipes are likely to occur under important mineral deposits such as Serra Pelada (Au, Pt, Pd) and Serra Leste (Fe), where magnetite-enriched iron formations occur.
- (iii) to outline areas of meta-mafic and meta-ultramafic rocks that contain PGE-mineralizations based on their Th radiometric signature (<10 cps; Fig. 9);
 - (iv) to map conductive domains down to depths of 300 and 400 m (Fig. 11), which is the depth limit of the GEOTEM system, that are coincident with known mafic-ultramafic complexes and banded iron formations;
 - (v) to delineate areas of granite occurrences based on their high values of total gamma radiation count, such as the Archean Estrela (2.76 Ga) and the Paleoproterozoic Cigano (1.88 Ga) granites (Fig. 8);
 - (vi) to map the main lineaments that outline tectonic compartments in the studied area. Gamma-ray spectrometry also suggest that radio elements are spatially distributed along structures associated with the Serra Pelada Divergent Splay. Displacements of lithostratigraphic units along shear zones were highlighted by these particular gamma-ray signatures;
 - (vii) the identification of specific geophysical signatures for the Luanga Cr-PGE deposit (high ASA, low Th and high electromagnetic conductivity); Serra Verde Cu–Au–Mo deposit (low ASA, high K and U; discrete electromagnetic conductivity) and Serra Pelada Au-PGE deposit (high ASA, high K, low Th and high electromagnetic conductivity); and
 - (viii) to establish a prospective model for the PGE-mineralizations in the Serra Leste region (Fig. 13), based on the integration and spatial modeling of geophysical and geological data.

Acknowledgments We are grateful to VALE (formerly CVRD) for providing the airborne geophysical data, access to the area and logistical support. C.R Souza Filho and R.P Xavier acknowledge FAPESP for financial support (Proc. 02/09038-6; Proc. 03/01996-6) and CNPq for the Research Grants (301.227/94; 300579/92-6). E.P Leite acknowledges FAPESP for the post-doctoral grant (Proc. No. 05/04453-3). A.M. Silva (University of Brasilia) is acknowledged for supporting A.R. Nunes in the early work on geophysical data processing and interpretation.

References

- Araújo OJB, Maia RGN, Jorge-João XS, Costa JBS (1988) A megaestruturação da folha Serra dos Carajás. 7 Congresso Latino Americano de Geologia, Proceedings, pp 324–333
- Avelar VG, Lafon JM, Correio JR, Macambira EMB (1999) O Magmatismo arqueano da região de Tucumã-Província Mineral de Carajás: novos resultados geocronológicos. *Revista Brasileira de Geociências* 29:454–460
- Barros CEM, Barbey P (2000) Significance of garnet-bearing metamorphic rocks in the Archean supra-crustal series of the Carajás Mining Province, Northern Brazil. *Rev Bras Geogr* 30(3):367–370
- Barros CEM, Sardinha AS, Barbosa JPO, Krimski R, Macambira MJB (2001) Pb–Pb and U–Pb zircon ages of Archean syntectonic granites of the Carajás metallogenic province, northern Brazil. 3 South American Symposium on Isotopic Geology, Proceedings. pp 94–97
- Barros CEM, Macambira MJB, Barbey P, Scheller T (2004) Dados isotópicos Pb–Pb em zircão (evaporação) e Sm–Nd do Complexo Granítico Estrela, Província Mineral de Carajás, Brasil: Implicações Petro-lógicas e Tectônicas. *Bol. Museu Paraense Emilio Goeldi* 34:531–538
- Blum MLB (1999) Processamento e interpretação de dados de geofísica aérea no Brasil central e sua aplicação à geologia regional e à prospecção mineral. Instituto de Geociências, Universidade de Brasília, Brasília, PhD Thesis, 229 pp
- Briggs IC (1974) Machine contouring using minimum curvature. *Geophysics* 39:39–48

- Cabral AR, Lehmann B, Kwitko R, Cravo CHC (2002a) The Serra Pelada Au–Pd–Pt deposit, Carajás Mineral Province, northern Brazil; reconnaissance mineralogy and chemistry of very high grade palladian gold mineralization. *Econ Geol* 97:1127–1138
- Cabral AR, Lehmann B, Kwitko R, Cravo CHC (2002b) Palladium and platinum minerals from the Serra Pelada Au–Pd–Pt deposit, Carajás Mineral Province, Northern Brazil. *Can Mineral* 40:1451–1463
- Coelho CES, Rodrigues OB (1986) Jazida de manganês do Azul, Serra dos Carajás, Pará. In: Schobbenhaus C, Coelho, CES (eds) Principais depósitos minerais do Brasil, Brasília, DNP/CVRD, vol 2, pp 145–152
- Cordell L, Grauch VJS (1985) Mapping basement magnetization zones from aeromagnetic data in the San Juan basin, New Mexico. In: Hinze WJ (ed) The utility of regional gravity and magnetic anomaly maps. Society of Exploration Geophysicists pp 181–97
- Dall’Agnol R, Lafon JM, Macambira MJB (1994) Proterozoic anorogenic magmatism In the Central Amazonian Province, Amazonian Craton: geochronological, petrological and geochemical aspects. *Mineral Petrol* 50:113–118
- Dall’Agnol R, Souza ZS, Althoff FJ, Barros CEM, Leite AAS, Jorge-João XS (1997) General aspects of the granitogenesis of the Carajás metallogenic province. Proceedings of the International Symposium on Granites and Associated Mineralizations, Salvador, Excursion Guide, pp 135–161
- Dall’Agnol R, Costi HT, Leite AA, Magalhães MS, Teixeira NP (1999a) Rapakivi granites from Brazil and adjacent areas. *Precambrian Res* 95:9–39
- Dall’Agnol R, Rämö OT, Magalhães MS, Macambira MJB (1999b) Petrology of the anorogenic, oxidised Jamon and Musa granites, Amazonian craton: implications for the genesis of Proterozoic A-type granites. *Lithos* 46:431–462
- Dall’Agnol R, Teixeira NP, Rämö OT, Moura CAV, Macambira MJB, Oliveira DC (2005) Petrogenesis of the Paleoproterozoic, rapakivi, A-type granites of the Archean Carajás Metallogenic Province, Brazil. *Lithos* 80:101–129
- Dalstra H, Guedes S (2004) Giant hydrothermal hematite deposits with Mg-Fe metasomatism: a comparison of the Carajás, Hamersley, and other iron ores. *Econ Geol* 99:1793–1800
- Debeglia N, Corpel J (1997) Automatic 3D interpretation of potential field data using analytic signal derivatives. *Geophysics* 62:87–96
- Dias GS, Macambira MB, Dall’Agnol R, Soares ADV, Barros CEM (1996) Datações de zircões de sill de metagabro: comprovação de idade arqueana da Formação Águas Claras, Carajás, Pará. Simpósio de Geologia da Amazônia, 5, Extended Abstracts, SBG, pp 376–378
- Dickson BL, Scott KM (1997) Interpretation of aerial gamma-ray surveys – adding the geochemical factors. In airborne magnetic and radiometric surveys. *AGSO J Aust Geol Geophys* 17:187–200
- Diella V, Ferrario A, Girardi VAV (1995) PGE and PGM in The Luanga mafic–ultramafic intrusion in Serra dos Carajás, Para States, Brazil. *Ore Geol Rev* 9:445–453
- Docegeo (1988) Revisão Litoestratigráfica Da Província Mineral De Carajás. In: SBG, Congresso Brasileiro de Geologia, 35, Belém, Anexo Aos Anais, pp 11–56
- Galarza TMA, Macambira MJB, Moura CAV (2003) Geocronologia Pb–Pb e Sm–Nd das rochas máficas do depósito Igarapé Bahia, Província Mineral de Carajás (PA) Simpósio de Geologia da Amazônia, 7, SBG [CD-ROM]
- Geomag (1993) Levantamento aéreo magnetométrico, gamaespectrométrico e eletromagnetométrico nas áreas Serra Pelada/Rio Novo e Almas (TO), Relatório final de aquisição, processamento e interpretação de dados. vol 1, 71 pp
- Geosoft (2000). OASIS Montaj™, v. 6.3.1(6G). GEOSOFT Inc, Toronto
- Girardi VAV, Ferrario A, Correia CT, Diella VA (2006) comparison of selected Precambrian Brazilian chromitites: chromite, PGE-PGM, and Re/Os as parental source indicators. *J South Am Earth Sci* 20:303–313
- Gunn PJ (1975) Linear transformations of gravity and magnetic fields. *Geophys Prospect* 23:300–312
- Gunn PJ, Minty BRS, Milligan PR (1997) The airborne gamma-ray spectrometric response over arid Australian Terrenes. In: Gubins AG (ed) Geophysics and geochemistry at the millennium. Proceedings of the fourth decennial International Conference on Mineral Exploration, pp 733–740
- Hirata WK, Rigon JC, Kadekaru K, Cordeiro AAC, Meireles EA (1982) Geologia regional da Província Mineral de Carajás. *Simp Geol Amaz*, 1, Belém, 1982 Anais Belém, SBG/NO, 1:100–110
- Holdsworth R, Pinheiro R (2000) The anatomy of shallow-crustal transpressional structures: insights from the Archean Carajás fault zone, Amazon, Brazil. *J Struct Geol* 22:1105–1123
- Hsu SK (2002) Imaging magnetic sources using Euler’s equation. *Geophys Prospect* 50:15–25
- Hsu SK, Sibuet JC, Shyu CT (1996) High-resolution detection of geological boundaries from potential-field anomalies: an enhanced analytical signal technique. *Geophysics* 61:373–386

- Huang L, Guan Z (1998) Discussion on “Magnetic interpretation using 3-D analytic signal” by Walter R. Roest, Jacob Verhoef and Mark Pilkington. *Geophysics* 63:667–670
- Huang L, Guan Z, Changli Y (1997) Comment on “An analytic signal approach to the interpretation of total field magnetic anomalies” by Shuang Qin. *Geophys Prospect* 45:879–881
- IAGA Division 5, Working Group 8 (1996) International geomagnetic reference field, 1995, revision. *Geophys J Int* 125:318–321
- Krymsky RS, Macambira JB, Macambira MJB (2002) Geocronologia U-Pb em zircão de rochas vulcânicas da formação Carajás, estado do Pará. In: Simpósio sobre Vulcanismo e Ambientes Associados, 2, Boletim de resumos e roteiro da excursão, 41 pp
- Li X (2006) Understanding 3D analytic signal amplitude. *Geophysics* 71(2):13–16
- Lobato LM, Roaière CA, Silva RCF, Zucchetti M, Baars FJ, Seoane JCS, Rios FJ, Pimentel M, Mendes GE, Monteiro AM (2005) A mineralização hidrotermal de ferro da Província Mineral de Carajás - controle estrutural e contexto na evolução metalogenética da Província. In: João Onildo Marini; Emanuel Teixeira de Queiróz; Waldir Benedito Ramos. (Org.). Caracterização de distritos mineiros da Amazônia. DNPM-CT-Mineral-ADIMB, Brasília, 2005, pp 25–92
- Macambira MJB, Lafon JM (1995) Geocronologia da Província Mineral de Carajás; síntese dos dados e novos desafios. *Boletim do Museu Paraense Emílio Goeldi* 7:263–288
- Machado N, Lindenmayer DH, Krough TE, Lindenmayer ZG (1991) U-Pb geochronology of Archean magmatism and basement reactivation in the Carajás area, Amazon Shield, Brazil. *Precambrian Res* 49:1–26
- Marschik R, Mathur RD, Spangenberg JE, Ruiz J, Leveille RA, Almeida AJ de (2001) The Serra Verde Cu-Mo-Au deposit, Carajás Mineral Province, Pará State, Brazil. Geological Society of America Annual Meeting, Boston, Abstracts and Programs, p A418
- Marschik R, Mathur R, Ruiz J, Leveille R, Almeida AJ de (2005) Late Archean Cu–Au–Mo mineralization at Gameleira and Serra Verde, Carajás Mineral Province, Brazil: constraints from Re-Os molybdenite ages. *Mineralium Deposita* 39:983–991
- Milligan PR, Gunn PJ (1997) Enhancement and presentation of airborne geophysical data. *AGSO-J Aust Geol Geophys* 17:63–76
- Minty BRS (1991) Simple microlevelling for aeromagnetic data. *Explor Geophys* 22:591–592
- Moroni M, Girardi VAV, Ferrario A (2001) The Serra Pelada Au-PGE deposit, Serra dos Carajás (Pará State, Brazil): geological and geochemical indications for a composite mineralising process. *Mineralium Deposita* 36:768–785
- Mougeot R, Respaut JP, Briquieu L, Ledru P, Milesi JP, Lerouge C, Marcoux E, Huhn SB, Macambira MJB (1996) Isotope geochemistry constraints for Cu, Au mineralizations and evolution of the Carajás Province (Para, Brazil). Congresso Brasileiro de Geologia, 39, Boletim de Resumos Expandidos, Sociedade Brasileira de Geologia vol 7, pp 321–324
- Nogueira ACR (1985) Análise faciológica e aspectos estruturais da Formação AguasClaras, região central da Serra dos Carajás. Master Thesis, Universidade Federal do Pará, Brazil
- Nunes AR (2002) Análise de dados geológicos, geofísicos e de sensoriamento remoto para geração de modelos prospectivos para a região de Serra Leste, Carajás (PA). Master Thesis, Universidade Estadual de Campinas, Brazil
- Pidgeon RT, Macambira MJB, Lafon JM (2000) Th-U-Pb isotopic systems and internal structures of complex zircons from an enderbite from the Pium Complex, Carajás Province, Brazil: evidence for the ages of granulite facies metamorphism and the protolith of the enderbite. *Chem Geol* 166:159–171
- Pimentel MM, Lindenmayer ZG, Laux JH, Armstrong R, Araújo JC (2003) Geochronology and Nd geochemistry of the Gameleira Cu–Au deposit, Serra dos Carajás, Brazil: 1.8–1.7 Ga hydrothermal alteration and mineralization. *J South Am Earth Sci* 15:803–813
- Pinheiro RVL, Holdsworth RE (1997) Reactivation of Archean strike-slip fault systems, Amazon region, Brazil. *J Geol Soc London* 154:99–103
- Reid AB, Allsop JM, Granser H, Millett AJ, Somerton IW (1990) Magnetic interpretation in three dimensions using Euler deconvolution. *Geophysics* 55:80–91
- Roest WR, Verhoef J, Pilkington M (1992) Magnetic interpretation using the 3-D analytical signal. *Geophysics* 57:116–125
- Sawatzky DL, Raines GL, Bonham-Carter GF, Looney CG, Souza Filho CR (2007) ARCSDM3.1: ArcMAP extension for spatial data modelling using weights of evidence, logistic regression, fuzzy logic and neural network analysis. <http://www.ige.unicamp.br/sdm/ArcSDM31/>
- Schaefer MJ, Gingerich J, Lemieux J (1998) Case study: the evolution of airborne time domain electromagnetic applications for geologic mapping: a Noranda perspective. *Explor Geophys* 29:204–210
- Siqueira JB (1996) Aspectos lito-estruturais e controle das mineralizações do depósito Salobo 3A. PhD Thesis, Universidade Federal do Pará, Belém, 157 pp

- Souza SRB, Macambira MJB, Sheller T (1996) Novos dados geocronológicos para os granitos deformados do Rio Itacaiúnas (Serra dos Carajás, PA); implicações estratigráficas. *Proceedings of the Simpósio de Geologia da Amazônia*, Belém, Brazil, pp 380–383
- Suita MTF (1988) Geologia da área Luanga com ênfase na petrologia do complexo básico-ultrabásico Luanga e depósitos de cromita associados, Pará. *Dissertação de Mestrado*, Brasília, UnB, 83 pp
- Suita MTF, Nilson AA (1988) Geologia do complexo máfico-ultramáfico Luanga (Província Mineral de Carajás, Pará) e das unidades encaixantes. *Cong Bras Geol*, 35, Belém 6:2813–2823
- Suita MTF, Hartmann LA, Fyfe WS (2005) Stratiform PGE + As-Rich chromitites from the Archean Luanga mafic-ultramafic complex (Carajás, Pará, Brazil). *Simpósio Brasileiro de Metalogenia*, 1, 2005, Gramado, Resumos Expandidos, [CD-ROM]
- Tallarico FHB, Coimbra CR, Costa CHC (2000) The Serra Leste sediment-hosted Au-(Pt-Pd) mineralization, Carajás Province. *Rev Bras Geoc* 30(2):226–229
- Tallarico FHB, Figueiredo BR, Groves DI, Kositsin N, McNaughton NJ, Fletcher IR, Rego JL (2005) Geology and SHRIMP U-Pb geochronology of the Igarape Bahia Deposit, Carajás copper-gold belt, Brazil, an Archean (2.57 Ga) example of iron-oxide Cu-Au-(U-REE) mineralization. *Econ Geol* 100:7–28
- Tallarico FHB, McNaughton NJ, Groves DI, Fletcher IR, Figueiredo BR, Carvalho BJ, Rego LJ, Nunes AR (2004) Geological and SHRIMP II U–Pb constraints on the age and origin of the Breves Cu–Au–(W–Bi–Sn) deposit, Carajás, Brazil. *Mineralium Deposita* 39:68–86
- Teixeira NP, Bettencourt JS, Moura CAV, Dall’Agnol R, Macambira EMB (2002) Archean crustal sources for Paleoproterozoic tin-mineralized granites in the Carajás Province, SSE Pará, Brazil: Pb–Pb geochronology and Nd isotope geochemistry. *Precambrian Res* 119:257–275
- Thompson DT (1982) EULDPH: a new technique for making computer-assisted depth estimates from magnetic data. *Geophysics* 47:31–37
- Thurston JB, Smith RS (1997) Automatic conversion of magnetic data to depth, dip, and susceptibility contrast using the SPI(TM) method. *Geophysics* 62(3):807–813
- Trendall AF, Basei MAS, De Laeter JR, Nelson DR (1998) SHRIMP U-Pb constraints on the age of the Carajás Formation, Grão Pará Group, Amazon Craton. *J South Am Earth Sci* 11:265–277
- Veneziani P, Okida R (2001) Mapeamento geológico-estrutural da região do Projeto Platina (Serra Pelada) baseado em dados integrados RADARSAT-TM-aerogeofísica. *Relatório Técnico*. Companhia Vale do Rio Doce, 52 pp
- Villas RN, Santos MD (2001) Gold deposits of the Carajás Mineral Province: deposit types and metallogenesis. *Mineralium Deposita* 36:300–333
- Wirth KR, Gibbs AK, Olszewski WJ (1986) U-Pb ages of zircons from the Grão Pará Group and Serra dos Carajás granite, Pará, Brasil. *Rev Bras Geoc* 16:195–200